Received 2 August 2019; revised 13 September 2019; accepted 22 September 2019. Date of publication 1 October 2019;
date of current version 6 December 2019. The review of this article was arranged by Editor M. Lemme.

Digital Object Identifier 10.1109/JEDS.2019.2944817

CJM: A Compact Model for Double-Gate Junction FETs

NIKOLAOS MAKRIS [1], MATTHIAS BUCHER [1] (Member, IEEE), FARZAN JAZAERI [2], AND JEAN-MICHEL SALLESE [2]

1 School of Electrical and Computer Engineering, Technical University of Crete, 73100 Chania, Greece
2 School of Engineering, Ecole Polytechnique Fédérale de Lausanne, CH 1015 Lausanne, Switzerland

CORRESPONDING AUTHOR: M. BUCHER (e-mail: bucher@electronics.tuc.gr)

This work was supported in part by the Project INNOVATION-EL Crete under Grant MIS 5002772.

ABSTRACT The double-gate (DG) junction field-effect transistor (JFET) is a classical electron device, with a simple structure that presents many advantages in terms of device fabrication but also its principle of operation. The device has been largely used in low-noise applications, but also more recently, in power electronics. Furthermore, co-integration of JFET with CMOS technology is attractive. Physics-based compact models for JFETs are however scarce. In this paper, an analytical, charge-based model is established for the mobile charges, drain current, transconductances and transcapacitances of symmetric DG JFETs, covering all regions of device operation, continuously from subthreshold to linear and saturation operation. This charge-based JFET model (called CJM) constitutes the basis of a full compact model of the DG JFET for analog, RF, and digital circuit simulation.

INDEX TERMS Charge-based model, CJM model, compact model, circuit simulation, depletion mode, double gate, high frequency, JFET, junction field effect transistor, low noise, Verilog-A.

I. INTRODUCTION

JFETs feature low noise, high input impedance and robust breakdown, which render them a preferred choice in a wide range of sensing applications, such as particle detectors [1], bioelectronics [2], microphones, RF circuitry [3], and more. Co-integration with CMOS technology [2]–[5] is considered due to the JFETs' low noise properties. JFETs are unipolar devices commonly operating in depletion mode (normally-on devices, with a negative threshold for n-JFETs). Ultra-scaled enhancement mode (normally-off), complementary JFETs (cJFETs) using silicon have been proposed for logic applications with channel lengths in the range of 25 nm - 10 nm [6]–[8] with gate voltage lower than 0.5 V to prevent a forward-bias of the channel-to-gate junction. For wide-bandgap semiconductors such as silicon carbide (SiC) [9], [10] or gallium nitride (GaN) [11], the gate voltage can be extended beyond 2V due to their high built-in voltage. JFET operation in below- and around-threshold regions, as needed for logic applications, as well as for positive gate voltage close to the built-in voltage, should therefore be revisited.

Compact models for JFETs have been loosely physics-based, and use empirical bridging among different operating regions [12]–[17]. Recently, a charge-based modeling approach [18]–[21] has resulted in a unified model of the symmetric DG JFET valid for gate voltage ranging from sub-threshold to above-threshold operation up to built-in voltage, and drain voltage from linear to saturation modes. The model approach also provides a full charges/transcapacitances model, which accounts for position-dependent charge distribution in the JFET channel and provides charge-conservation in transient simulation [19].

In the present work, the foundations of the charge-based JFET model - henceforth designated as CJM - are re-visited. A normalization procedure of physical quantities provides new insight into the principle of operation of the depletion mode JFET. The present paper gives a detailed validation of CJM, for fundamental device behavior, based on comparison to technology computer-aided design (TCAD) simulations, as well as to measured experimental characteristics of silicon JFETs. Drain current,

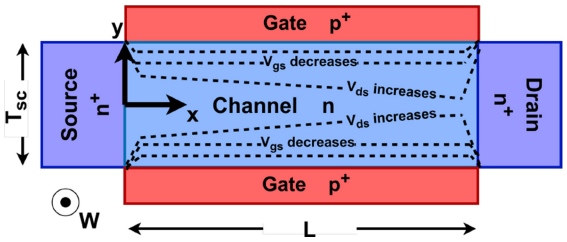

FIGURE 1. Schematic of the Double Gate Junction FET. The JFET's channel thickness, width and length are T_{sc}, W and L, respectively.

TABLE 1. Model parameters of long-channel DG JFET.

Parameter	Unit	Value	Description
N_D	cm^{-3}	10^{17}	Channel doping concentration
N_A	cm^{-3}	10^{19}	Gate doping concentration
T_{sc}	m	$500 \cdot 10^{-9}$	Channel thickness
ε_r	$-$	11.7	Material relative permittivity
ε_0	Fm^{-1}	$8.85{\cdot}10^{-12}$	Vacuum permittivity
L	m	$4 \cdot 10^{-5}$	Channel length
W	m	10^{-6}	Channel width
$\mu_0(25^oC)$	$(cm^2)/Vs$	1000	Carrier low field mobility
$n_i(25^oC)$	cm^{-3}	$1.45 \cdot 10^{10}$	Intrinsic concentration

transconductances, transconductance-to-current ratio, transcapacitances and unity gain frequency (F_T), are shown to be directly related to mobile charge density at source and drain. These large- and small-signal quantities are highly important in analog/RF integrated circuit design but will also cover needs for digital design using complementary JFETs. The CJM model is coded in Verilog-A [22] to ensure portability among circuit simulators.

II. CHARGE BASED MODEL OF THE JFET

A. DRAIN CURRENT

Considering an n-type Double Gate (DG) JFET, shown in Fig. 1, with channel thickness T_{sc}, device width W, device length L, channel doping concentration N_D and gate doping concentration N_A, the local channel current is calculated as in [18] using the drift-diffusion model,

$$I_{ds} = -\mu W Q_m \, {}^{\partial V}/_{\partial x}, \tag{1}$$

where μ is the electron mobility and Q_m is the (local) mobile charge density (per unit area) which is expressed as $Q_m = -Q_f + Q_{sc}$, where Q_{sc} is the total (local) charge density (per unit area) in the semiconductor channel, and $Q_f = qT_{sc}N_D$ is the fixed charge density (per unit area), which is constant throughout the channel. The device parameters given in Table 1 are used for the numerical simulations as well as for the analytical model evaluations. The simulations are performed in Silvaco Atlas device simulator [23]. The device is a long-channel ($L = 40um$) symmetric Double Gate JFET at room temperature. The mobility is considered constant and uniform along the channel. A refined mesh at the center of the device is used due to volume transport.

In the following, a normalization scheme is introduced, similarly as used in the context of models for, e.g., single-gate MOSFETs [24] and HEMTs [25]. This procedure does not alter the physical relationships, it allows us however to write relationships in a more dense way, presenting many advantages, e.g., in terms of analysis, circuit design and parameter extraction (see Section II-C). The normalization quantities and normalization procedure are summarized in Table 2. Other quantities that are frequently used in the model are presented in Table 3.

TABLE 2. Normalization quantities.

Quantities	Normalization Quantities	Normalized Values
Voltage	$U_T = kT/q$	$v = V/U_T$
Charge Density	$Q_f = qT_{sc}N_D$	$q_m = Q_m/Q_f$ $q_{sc} = Q_{sc}/Q_f$
Total Charge	$Q_{spec} = WLQ_f$	$q_r = Q_r/Q_{spec}$
Capacitance	$C_{spec} = Q_{spec}/U_T$	$c_{wz} = C_{wz}/C_{spec}$
Current	$I_{spec} = \mu \frac{W}{L} Q_f U_T$	$i = I/I_{spec}$
Transconductance	$G_{spec} = I_{spec}/U_T$	$g_m = G_m/G_{spec}$
Distance along channel	L	$\xi = x/L$

TABLE 3. Frequently used quantities.

$b = 8qN_D\varepsilon_{sc}$
$V_p = Q_f^2/b = qT_{sc}^2N_D/(8\varepsilon_{sc})$
$V_{ni} = qT_{sc}^2n_i/(8\varepsilon_{sc})$
$V_F = U_T ln\,(N_A/n_i)$
$V_{ch} = U_T ln\,(N_D/n_i)$
$V_{bi} = V_F + V_{ch} = U_T ln\,(N_D N_A/n_i^2)$

The total charge density is defined in [18] as

$$\begin{aligned} Q_{sc} &= Q_f + Q_m = \sqrt{b(\Psi_o - \Psi_s)} \Leftrightarrow \\ Q_f q_{sc} &= Q_f(1+q_m) = \sqrt{bU_T(\psi_o - \psi_s)} \Leftrightarrow \\ q_{sc} &= 1 + q_m = \sqrt{\frac{\psi_o - \psi_s}{v_p}} \end{aligned} \tag{2}$$

where q_{sc} is the normalized total local charge ranging from 1 (deep depletion) to 0 (flat band condition), q_m is the normalized mobile charge ranging from 0 (deep depletion) to -1 (flat band condition), ψ_0 and ψ_s are the normalized potentials at the center of the channel and at the interface between the channel and the gate, respectively, and $v_p = V_p/U_T$ is the normalized pinchoff voltage.

As long as the junction between gate and channel is abrupt and one-sided, Ψ_s is considered equal to $\Psi_s = V_g - V_F$ where V_F is the gate Fermi potential. Ψ_o is calculated as [26],

$$\begin{aligned} \Psi_o &= \Psi_s + V_p - U_T L_W\left(v_{ni}e^{(\psi_s + v_p - v)}\right) \Leftrightarrow \\ \psi_o &= \psi_s + v_p - L_W\left(v_{ni}e^{(\psi_s + v_p - v)}\right) \end{aligned} \tag{3}$$

where $v_{ni} = V_{ni}/U_T$, and n_i is the intrinsic carrier concentration. L_W is the Lambert W function, which is efficiently implemented as,

$$L_W(z) \cong \ln(1+z)\left(1 - \frac{\ln(1+\ln(1+z))}{2+\ln(1+z)}\right). \tag{4}$$

Henceforth, the mobile charge is directly calculated combining (3) and (2). In turn, the charge-potential relation is

obtained substituting (3) in (2) and reverting it,

$$V_g - V - V_{bi} = -\frac{Q_{sc}^2}{b} + U_T \ln\left(-\frac{Q_{sc}^2}{Q_f^2} + 1\right) \Leftrightarrow$$
$$U_T(v_g - v - v_{bi}) = -\frac{Q_f^2}{b} q_{sc}^2 + U_T \ln\left(-\frac{Q_f^2 q_{sc}^2}{Q_f^2} + 1\right) \Leftrightarrow$$
$$v_g - v - v_{bi} = -v_p q_{sc}^2 + \ln\left(-q_{sc}^2 + 1\right) \quad (5)$$

where $v_{bi} = V_{bi}/U_T$ is the normalized built-in potential. Note the similarities with [24]. Upon substituting q_{sc} with $q_m + 1$, (5) may be rewritten,

$$v_g - v - v_{bi} + v_p = -v_p q_m(q_m + 2) + \ln(-q_m(q_m + 2)) \quad (6)$$

The threshold voltage is determined from (6) considering the mobile charge zero and ignoring the logarithmic term,

$$V_{th} \cong V_{bi} - V_p. \quad (7)$$

The derivative form of (6) in normalized quantities is expressed as,

$$dv = \left[2v_p(q_m + 1) - \frac{2(q_m + 1)}{q_m(q_m + 2)}\right] dq_m. \quad (8)$$

The first term of the right hand side of (8) is the drift term and the second is the diffusion term.

The drain current is obtained by integrating (1) along the channel,

$$I_{ds} = -\mu \frac{W}{L} \int_{V_s}^{V_d} Q_m dv = -\mu \frac{W}{L} \int_{v_s}^{v_d} Q_f q_m U_T dv$$
$$= -I_{spec} \int_{v_s}^{v_d} q_m dv. \quad (9)$$

Substituting dv in (9) with (8) and integrating, the current becomes,

$$I_{ds} = I_{spec}(i_{ms} - i_{md})$$
$$i_{ds} = i_{ms} - i_{md} \quad (10)$$

where i_m is evaluated at source and drain,

$$i_m = \frac{2}{3} v_p q_m^3 + v_p q_m^2 - 2q_m + 2ln(q_m + 2). \quad (11)$$

Interestingly, we note that the diffusion term in (8) tends to $1/q_m$ when $q_m \to 0$. So, (8) becomes,

$$dv \cong \left[2v_p(q_m + 1) - \frac{1}{q_m}\right] dq_m. \quad (12)$$

Performing the integration in (9) using (12), i_m is approximated as,

$$i_m \cong \frac{2}{3} v_p q_m^3 + v_p q_m^2 - q_m. \quad (13)$$

The drain current obtained using (13) instead of (11) deviates less than 1% in all regions of operation (sub- to above-threshold and linear to saturation) which fully justifies this simplification. This simplification with respect to [18] alleviates the computational burden, but also allows for an easier interpretation of device physics: The quadratic and cubic terms of mobile charge correspond to drift transport, while the linear term of mobile charge corresponds to diffusion transport.

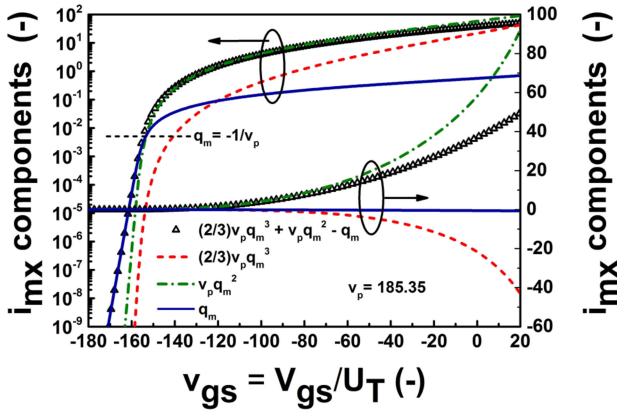

FIGURE 2. Normalized current components i_m versus gate voltage. The linear (q_m) and quadratic (q_m^2) terms of mobile charge are seen to dominate sub- and above-threshold regions, respectively, while the cubic term (q_m^3) is important at high gate voltage.

As demonstrated in Fig. 2, the linear mobile charge term dominates drain current in subthreshold region. At the transition from diffusion to drift, the linear and quadratic mobile charge terms are equal and $q_{m,th} = -1/v_p$ ($i_{m,th} = 2/v_p$). As the gate voltage increases, the quadratic term first prevails, while at even higher gate voltage, the cubic term gradually starts to counterbalance the current increase due to the quadratic term, as shown in the same figure.

In subthreshold region, the current is expressed directly from the mobile charges as,

$$i_{ds,diffusion} \cong -q_{ms} + q_{md} \quad (14)$$

In above-threshold conditions,

$$i_{ds,drift} \cong \frac{2}{3} v_p q_m^3 + v_p q_m^2 \Big|_{q_{md}}^{q_{ms}} \quad (15)$$

where the quadratic and cubic terms prevail.

B. TRANSCONDUCTANCES

The transconductances are calculated as the partial derivatives of the current with respect to the gate, source or drain voltages,

$$G_{mx} = \frac{\partial I_{ds}}{\partial V_x} = \frac{I_{spec}}{U_T} \frac{\partial i_{ds}}{\partial v_x} = G_{spec} \frac{\partial i_{ds}}{\partial v_x} \Leftrightarrow$$
$$g_{mx} = \frac{\partial i_{ds}}{\partial v_x} = \frac{\partial i_{ds}}{\partial q_{mx}} \frac{\partial q_{mx}}{\partial v_x} \quad (16)$$

where $x = d, s$. Hence, source and drain transconductances are expressed as,

$$g_{ms} = \frac{\partial i_{ds}}{\partial q_{ms}} \frac{\partial q_{ms}}{\partial v_s} = q_{ms}, \; g_{md} = \frac{\partial i_{ds}}{\partial q_{md}} \frac{\partial q_{md}}{\partial v_d} = -q_{md} \quad (17)$$

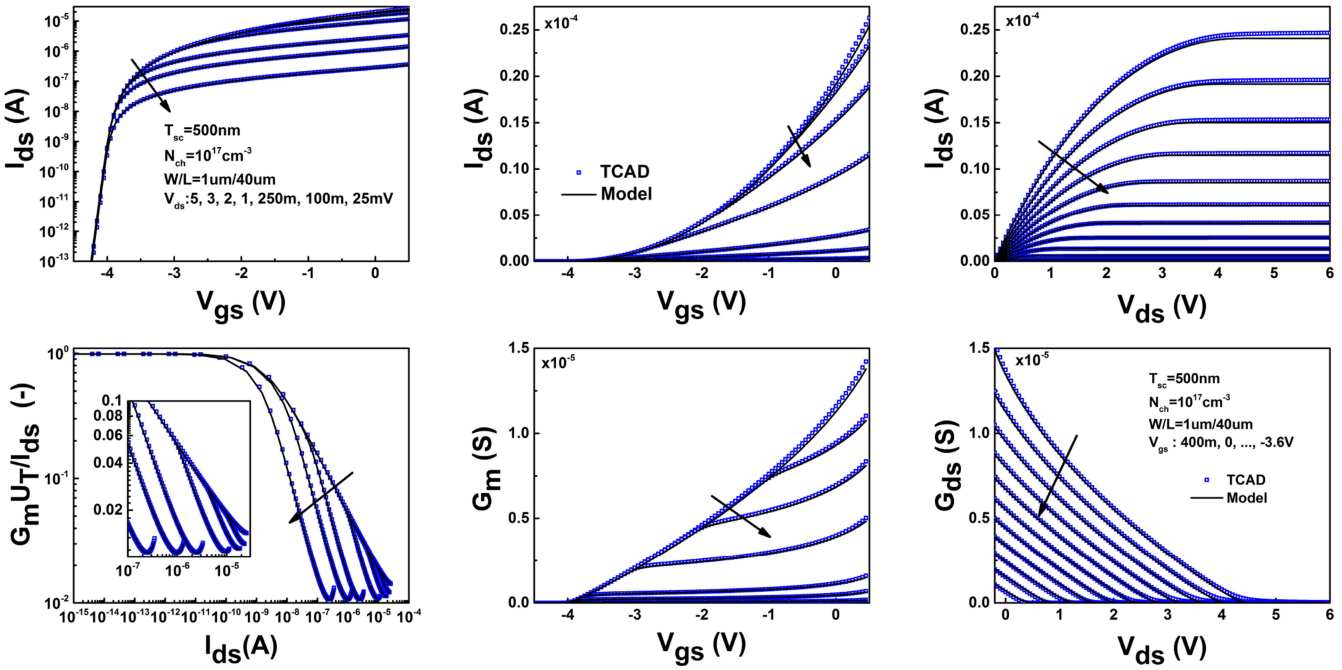

FIGURE 3. Transfer and output characteristics of a long-channel DG n-JFET, at $T = 25^oC$, including transconductances and transconductance-to-current ratio. The TCAD simulation (markers) and the analytical model (lines) use the same parameters (see Table 1).

which is a result that can indeed be expected from (1). Accordingly, the gate transconductance is calculated as,

$$g_m = \frac{\partial i_{ds}}{\partial v_g} = \frac{\partial i_{ms}}{\partial q_{ms}}\frac{\partial q_{ms}}{\partial v_g} - \frac{\partial i_{md}}{\partial q_{md}}\frac{\partial q_{md}}{\partial v_g} = q_{md} - q_{ms}. \quad (18)$$

In saturation, when $q_{md} \cong 0$, the normalized gate transconductance becomes $g_{m,sat} \cong -q_{ms}$.

Transfer and output characteristics including transconductances are illustrated in Fig. 3 as compared to numerical simulations. The correspondence of the analytical model with numerical simulations is appreciable given that no parameter fitting is involved.

C. TRANSCONDUCTANCE-TO-CURRENT RATIO

The transconductance-to-current ratio is an important indicator as to the efficiency of a device to produce transconductance at a given current, and constitutes an important quantity for analog circuit design. g_m/i_{ds} can be analytically expressed in terms of mobile charge,

$$\frac{G_m U_T}{I_{ds}} = \frac{G_{spec} U_T}{I_{spec}}\frac{g_m}{i_{ds}} = \frac{g_m}{i_{ds}} = \frac{1}{1 - v_p\left((2/3)\left(q_{ms}^2 + q_{ms}q_{md} + q_{md}^2\right) + q_{ms} + q_{md}\right)} \quad (19)$$

In subthreshold $q_m \to 0$, hence (19) approaches $g_m/i_{ds} \cong 1$, which is equivalent to an ideal subthreshold slope. In saturation, the drain side is considered fully depleted, $q_{md} \cong 0$, (19) becomes,

$$\left.\frac{g_m}{i_{ds}}\right|_{sat} = \frac{1}{1 - v_p\left((2/3)q_{ms}^2 + q_{ms}\right)} \quad (20)$$

In linear mode and assuming $q_{ms} \cong q_{md}$,

$$\left.\frac{g_m}{i_{ds}}\right|_{lin} = \frac{1}{1 - 2v_p\left(q_{ms|d}^2 + q_{ms|d}\right)} \quad (21)$$

The transconductance-to-current ratio can hence be expressed as a function of mobile charge, similarly as in MOSFETs. The analytical expressions of g_m/i_{ds} in linear mode and saturation match numerical simulations perfectly well as shown in Fig. 4 The two devices have different threshold voltage, while the subthreshold slope remains the same. The upward-bending of g_m/i_{ds} at high current, which is most prominent in linear mode (see also Fig. 3, already observed in TCAD and experiment [20]) is clearly attributed to the second-order mobile charge terms in (19) - (21).

An interesting point to consider is the normalized transconductance-to-current ratio when drift and diffusion currents are equal as noted in Section II-A. In saturation and at that point, only the first-order mobile charge term in (20) is important and setting $q_{m,th}$=-1/v_p, we obtain,

$$\left.\frac{g_m}{i_{ds}}\right|_{v_{th}} \cong \frac{1}{1 - v_p q_{ms,th}} = \frac{1}{2} \quad (22)$$

This particular condition $g_m/i_{ds} \cong 1/2$ corresponds to the threshold condition, similar as in junctionless nanowire transistors [27].

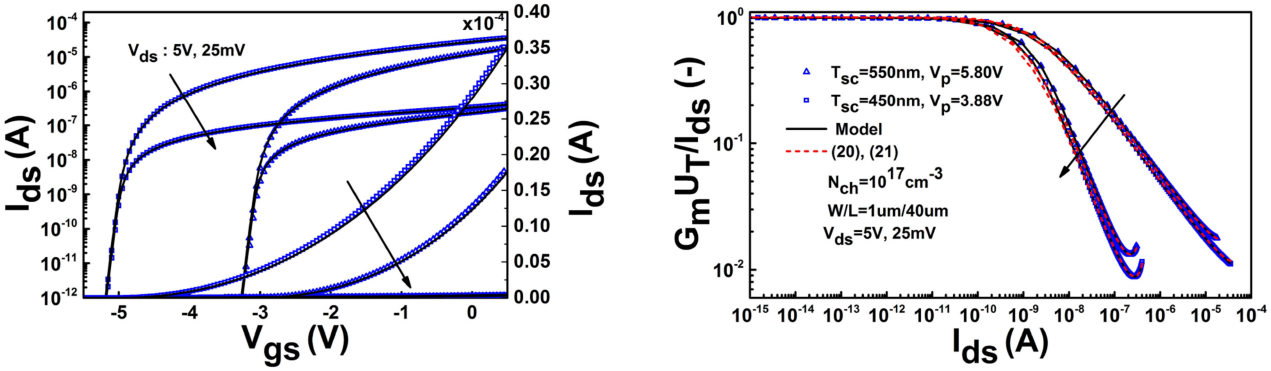

FIGURE 4. Drain current and transconductance-to-current ratio in linear and saturation modes, for two different values of T_{SC} (otherwise same parameters as in Table 1). Markers: TCAD data, lines: model, dashed: analytical expressions (g_m/i_{ds}). While the two devices show vastly different threshold voltage, their transconductance-to-current ratio versus drain current is very similar.

D. TOTAL CHARGES AND TRANSCAPACITANCES

The total gate charge Q_G is obtained by integrating the mobile charge along the channel,

$$\begin{aligned} Q_G &= -(Q_D + Q_S) = -W\int_0^L Q_m dx \\ &= -W\int_0^1 Q_f q_m L d\xi = -Q_{spec}\int_0^1 q_m d\xi \Leftrightarrow \\ q_G &= -(q_D + q_S) = -\int_0^1 q_m d\xi \end{aligned} \tag{23}$$

where $\xi = x/L$ is the normalized position along the channel. The drain and source total normalized charges are obtained using Ward-Dutton's linear partitioning scheme, as in [19],

$$q_D = \int_0^1 \xi\, q_m d\xi,\ \ q_S = \int_0^1 (1-\xi) q_m d\xi \tag{24}$$

Using current continuity, we obtain the normalized form,

$$\xi = \frac{i_m - i_{ms}}{i_{md} - i_{ms}} \tag{25}$$

Differentiating (25) and assuming drift transport yields $di_m/dq_m \cong 2v_p(q_m^2 + q_m)$ and we obtain,

$$\begin{aligned} d\xi &= \frac{1}{i_{md} - i_{ms}} di_m = \frac{1}{i_{md} - i_{ms}} \frac{di_m}{dq_m} dq_m \\ &\cong \frac{2v_p(q_m^2 + q_m)}{i_{md} - i_{ms}} dq_m \end{aligned} \tag{26}$$

Hence, the integrals (23), (24) can be calculated. The full expressions for total charges [19] are quite complex. Useful asymptotic expressions are obtained in linear mode using $q_{md} \cong q_{ms}$,

$$q_{G,lin} = -q_m\ \ q_{S,lin} = q_{D,lin} = \frac{q_m}{2} \tag{27}$$

while in saturation, using $q_{md} = 0$,

$$q_{G,sat} = \frac{-q_{ms}(3q_{ms} + 4)}{2(2q_{ms} + 3)} \tag{28}$$

$$q_{S,sat} = \frac{q_{ms}\left(60q_{ms}^2 + 175q_{ms} + 126\right)}{35(2q_{ms} + 3)^2} \tag{29}$$

$$q_{D,sat} = \frac{q_{ms}\left(90q_{ms}^2 + 245q_{ms} + 168\right)}{70(2q_{ms} + 3)^2}. \tag{30}$$

The transcapacitances are then obtained by partially differentiating the total charges (23), (24) with respect to terminal voltages. The transcapacitances c_{gs}, c_{gd}, c_{ds}, c_{dd}, c_{sd} and c_{ss} are calculated as,

$$C_{wz} = \pm\frac{\partial Q_w}{\partial V_z} = \pm\frac{Q_{spec}}{U_T}\frac{\partial q_w}{\partial v_z} \Leftrightarrow c_{wz} = \pm\frac{\partial q_w}{\partial q_{mz}}\frac{\partial q_{mz}}{\partial v_z}, \tag{31}$$

where w is G, S or D and z is S or D. Plus sign is assigned when w=z and minus otherwise. The remaining transcapacitances c_{gg}, c_{sg} and c_{dg} are obtained as in [19],

$$c_{gg} = c_{gs} + c_{gd},\ \ c_{sg} = c_{ss} - c_{sd},\ \ c_{dg} = c_{dd} - c_{ds} \tag{32}$$

Similarly as for total charges, the full expressions of transcapacitances may also be simplified in asymptotic regions, e.g., in above-threshold operation [19]. Here, transcapacitances including subthreshold region are described, for linear mode as well as saturation, which are of particular interest.

In linear mode, $q_{md} \cong q_{ms}$ and therefore, all nine transcapacitances are obtained as,

$$\begin{aligned} c_{gg,lin} &= 2c_{gs(gd)} = 2c_{sg(dg)} = 3c_{dd(ss)} = -6c_{ds(sd)} \\ &= \frac{q_m}{2v_p q_m^2 + 2v_p q_m - 1} \end{aligned} \tag{33}$$

In saturation, considering $q_{md} \cong 0$, three transcapacitances are obtained,

$$c_{gg,sat} = \frac{3q_{ms}(q_{ms}+1)(q_{ms}+2)}{\left(2v_p q_{ms}^2 + 2v_p q_{ms} - 1\right)(2q_{ms}+3)^2} \tag{34}$$

$$c_{sg,sat} = \frac{6q_{ms}(q_{ms}+1)\left(20q_{ms}^2 + 70q_{ms} + 63\right)}{35\left(2v_p q_{ms}^2 + 2v_p q_{ms} - 1\right)(2q_{ms}+3)^3} \tag{35}$$

$$c_{dg,sat} = \frac{9q_{ms}(q_{ms}+1)\left(10q_{ms}^2 + 35q_{ms} + 28\right)}{35\left(2v_p q_{ms}^2 + 2v_p q_{ms} - 1\right)(2q_{ms}+3)^3} \tag{36}$$

while $c_{gs,sat} = c_{gg,sat}$, $c_{ss,sat} = c_{sg,sat}$, $c_{ds,sat} = c_{dg,sat}$. In saturation, the drain side is considered fully depleted resulting

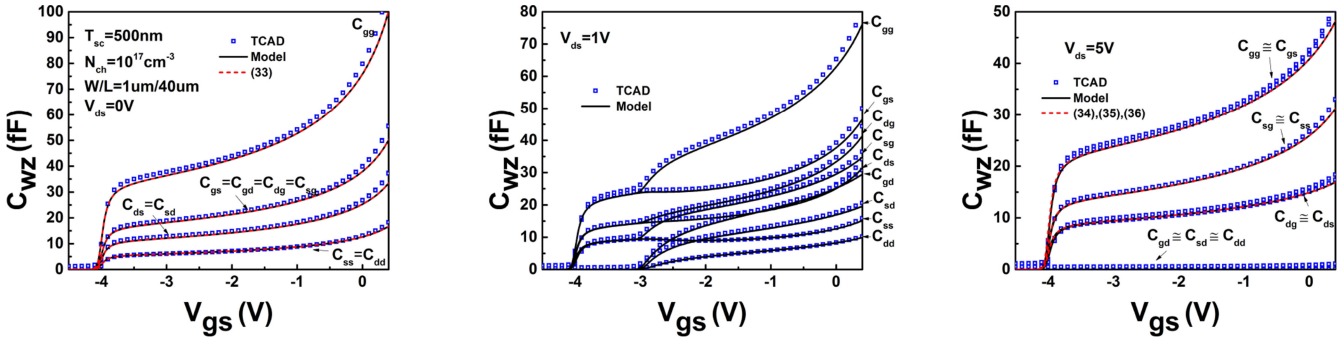

FIGURE 5. Intrinsic Transcapacitances (absolute values) versus gate voltage of a long-channel DG n-JFET, at $T = 25^oC$, for three different drain voltages. Markers: TCAD data, lines: model, dashed: analytical expressions.

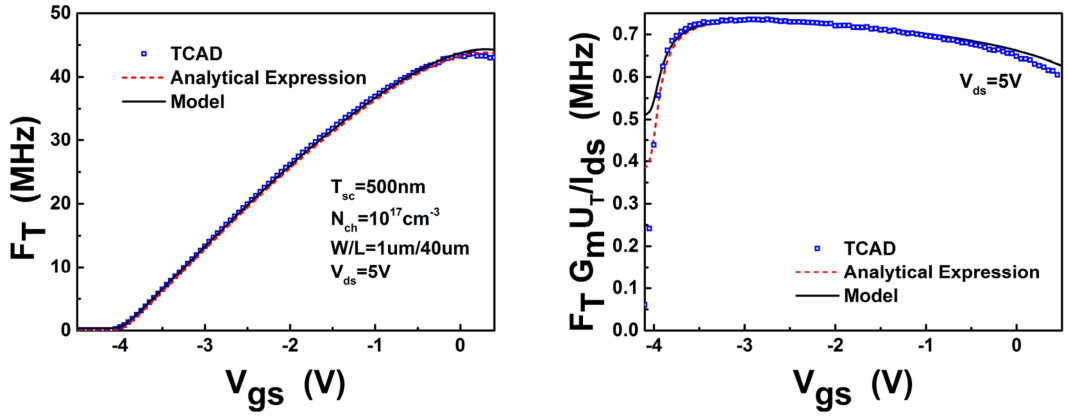

FIGURE 6. Transit frequency F_T and RF Figure-of-Merit (FOM) $FoM_{RF} = F_T G_m U_T / I_{ds}$ versus gate voltage, for a long-channel ($L = 40\mu m$) DG n-JFET, at $T = 25^oC$. Markers: TCAD data, line: model, dashed: analytical expression.

in $c_{gd,sat} = c_{sd,sat} = c_{dd,sat} = 0$. Transcapacitance in saturation and above threshold may be simplified [19], considering $q_{md} = 0$,

$$c_{gg,sat} = c_{gs,sat} \cong \frac{3}{2v_p}\frac{q_{sc,s}+1}{(2q_{sc,s}+1)^2} = \frac{3}{2v_p}\frac{q_{ms}+2}{(2q_{ms}+3)^2} \quad (37)$$

where $q_{sc,s}$, above threshold, is approximated as,

$$\begin{aligned} Q_{sc,d(s)}\big|_{drift} &\cong \sqrt{b\left(V_{bi} - V_{gd(s)}\right)} \Leftrightarrow \\ q_{sc,d(s)}\big|_{drift} &\cong \sqrt{\frac{v_{bi}-v_{gd(s)}}{v_p}} \end{aligned} \quad (38)$$

In Fig. 5, the model and TCAD-simulated transcapacitances are shown versus gate voltage at various drain voltages. A very good agreement is observed at all bias conditions, including the transition regions from saturation to non-saturation, and at high gate voltage. Note that so far, no other complete compact models have been presented to cover position- and bias-dependence of total charges and transcapacitances in JFETs. The consistent estimation of charges in the device guarantees charge-conservation during time-domain circuit simulation. The transcapacitances model opens new perspectives for high-frequency applications of JFETs.

E. TRANSIT FREQUENCY

Transit frequency F_T is an important RF performance metric corresponding to the frequency at which the the common-source current gain of a transistor becomes unity. F_T is obtained from small-signal evaluation of Y-parameters, at a moderate frequency F_0,

$$F_T = \frac{F_0}{Im(Y_{11}/Y_{21})} \cong \frac{G_m}{2\pi C_{GG}} \underset{sat}{=} \frac{\mu_0 U_T}{2\pi L^2}\frac{g_{m,sat}}{c_{gg,sat}} \quad (39)$$

When using $g_{m,sat}$=$-q_{ms}$ and $c_{gg,sat}$ given by (34), the transit frequency is expressed solely in terms of the mobile charge at the source q_{ms},

$$F_T \cong -\frac{\mu_0 U_T}{2\pi L^2}\frac{\left(2v_p q_{ms}^2 + 2v_p q_{ms} - 1\right)(2q_{ms}+3)^2}{3(q_{ms}+1)(q_{ms}+2)} \quad (40)$$

In Fig. 6, the analytical equation (40) is compared to F_T from TCAD and circuit simulation using the full model, both obtained from small-signal Y-parameters, using same parameters as in previous figures. Furthermore, Fig. 6 shows the RF figure-of-merit FoM_{RF} defined as,

$$FoM_{RF} = F_T \frac{G_m U_T}{I_{ds}} = F_T \frac{g_m}{i_{ds}} \quad (41)$$

which is indicative of ideal biasing for low-power, low-noise, high-frequency applications. FoM_{RF} may again explicitly

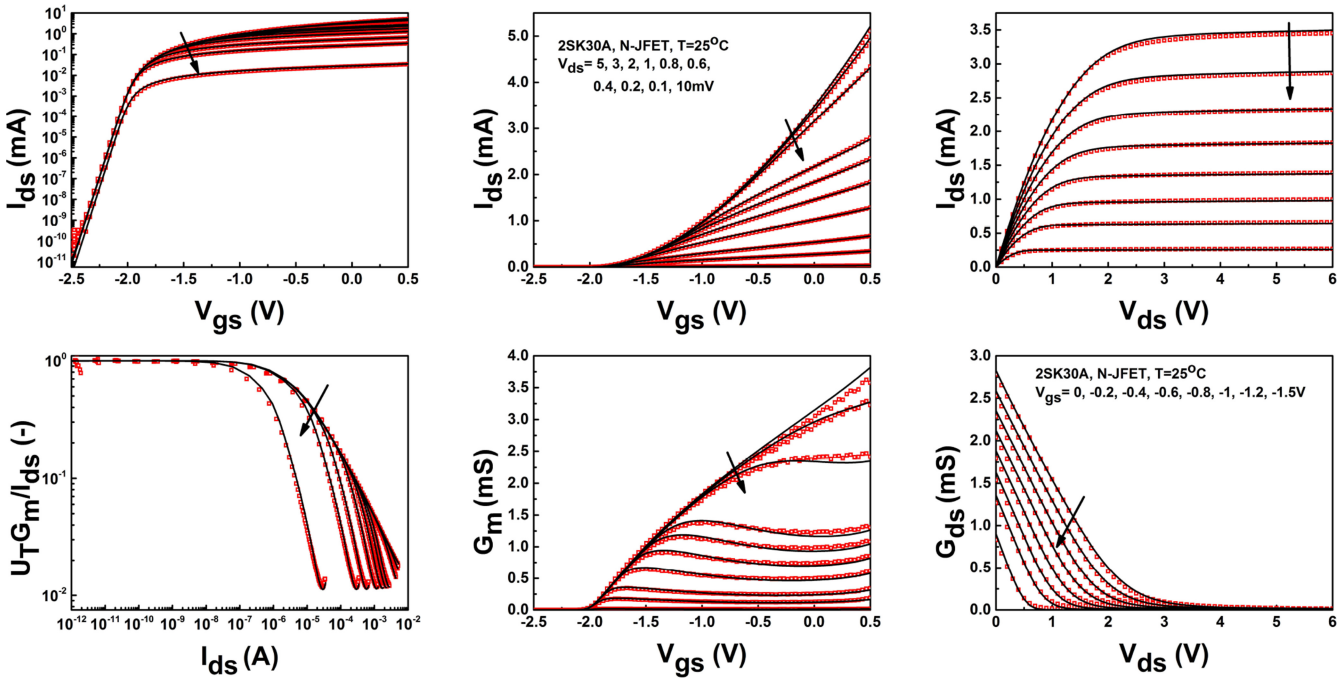

FIGURE 7. Transfer and output characteristics of an n-channel JFET (2SK30A), at $T = 25^oC$, including transconductances and transconductance-to-current ratio. Markers: measurements, lines: CJM model.

be expressed in terms of mobile charge at the source q_{ms} using (20) and (40),

$$FoM_{RF} = \frac{\mu_0 U_T}{2\pi L^2} \frac{\left(2v_p q_{ms}^2 + 2v_p q_{ms} - 1\right)(2q_{ms} + 3)^2}{\left(2v_p q_{ms}^2 + 3v_p q_{ms} - 3\right)(q_{ms} + 1)(q_{ms} + 2)} \tag{42}$$

FoM_{RF} culminates at a gate voltage slightly above threshold voltage. Velocity saturation-related effects in short-channel devices will move this point even closer to threshold. The model and the analytical expressions for F_T and FoM_{RF} coincide and give a good qualitative fit to the TCAD data in Fig. 6, given that no model parameters are adjusted.

III. MODEL EXTENSIONS AND EXPERIMENTAL

In the present Section, the modeling of second-order effects is introduced. Velocity saturation is the most prominent of short-channel effects. A comparison of the CJM model with measured characteristics from silicon JFETs is then provided.

A. VELOCITY SATURATION

Considering the effect of velocity saturation in mobility, following similar procedures as in [25], we assume,

$$i_{ds} = -u q_m \, {}^{dv}/_{d\xi}, \tag{43}$$

where $u = \mu_{eff}/\mu_o = 1/(1 + e)$ and $e = E/E_{crit}$.

The derivative in turn is written,

$$dq_m = \frac{1}{2\sqrt{v_p(\psi_o - \psi_s)}} \frac{d\psi_o}{d\xi} = \frac{1}{2v_p(q_m + 1)} \frac{d\psi_o}{d\xi}. \tag{44}$$

The lateral field $E_x = \partial\psi_o/\partial x$ is calculated as,

$$e = \frac{E_x}{E_{crit}} = \frac{U_T}{E_{crit} L} \frac{d\psi_o}{dx} = 2\lambda_c v_p [q_m + 1] \frac{\partial q_m}{\partial \xi} \tag{45}$$

where $\lambda_c = U_T/(E_{crit}L)$ and E_{crit} is the critical field for velocity saturation. Hence,

$$i_{ds}(1 + 2\lambda_c v_p [q_m + 1] \frac{dq_m}{d\xi}) d\xi = -q_m dv. \tag{46}$$

Integrating (46) from drain to source we obtain

$$i_{ds} = \frac{i_{ms} - i_{md}}{1 + 2\lambda_c v_p (0.5 q_m^2 + q_m)_s^d}. \tag{47}$$

The mobile charge in saturation, q_{msat}, is determined from the third degree polynomial numerator of g_{ds}, considering the saturation condition, $g_{ds} = \partial i_{ds}/\partial v_{ds} = 0$, and using the conduction (quadratic and cubic) terms of i_m. A limited Newton-Raphson like method, avoiding iterations, is used to calculate q_{msat}.

The channel length modulation (CLM) effect is responsible for the prominent degradation of output conductance in saturation, which is closely related to velocity saturation. The model implemented follows principles in [28]. Details of model formulation of CLM and other short-channel effects will be provided elsewhere.

B. EXPERIMENTAL EVALUATION

Fig. 7 shows measured transfer and output characteristics of a commercial n-type JFET [29], as well as the results obtained with the CJM model. Model parameters were extracted to fit measured characteristics, while using estimated values for geometries of the device, which are not

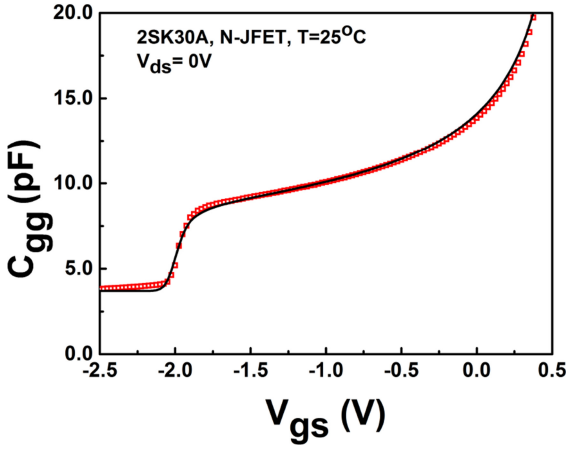

FIGURE 8. Two terminal capacitance versus gate voltage of an n-channel JFET (2SK30A), at $T = 25^oC$. Markers: measurements, line: CJM model.

provided by the manufacturer. Drain current, transconductances, transconductance-to-current ratio are well modeled. Note the ideal subthreshold slope featured experimentally. The model covers drain current also in the region of positive gate bias. Transconductances (and transconductance-to-current ratio) are well modeled in sub- to above-threshold regions as well as from linear to saturation operation. Velocity saturation, channel length modulation and series resistance have been accounted for in the model. Source and drain series resistances are handled as bias-independent, lumped resistors. Fig. 8 provides a validation of the capacitance characteristics versus measured data, for the same device as in Fig. 7. A constant subthreshold capacitance term was added to allow for a validation of the model versus the measured capacitance. An evaluation of the model for SiC and GaN JFETs has been provided in [30], including at high temperatures. Finally, the model is available as an online tool called JFETlab [31].

IV. CONCLUSION

A unified charge-based model of the of the depletion mode, symmetric, double-gate JFET called CJM valid in all regions of operation has been presented. The model covers large- and small-signal effects from subthreshold to above threshold, and from linear mode to saturation. Drain current, transconductances, total charges, transcapacitances are all expressed as analytical and continuous functions of mobile charge at source and drain. The analytical structure of the model, combined with a normalization procedure, provides insight into the physical behavior of the device in different operating regions. The current-charge relationship is simplified with respect to former formulations. Analog/RF figures of merit such as g_m/i_d ratio, transcapacitances, transit frequency F_T etc. can be expressed in a very compact way in terms of mobile charges. Second-order effects such as velocity saturation have been discussed. The CJM model has been validated with respect to TCAD simulation as well as measurements from silicon JFETs. The model is coded in Verilog-A for ease of portability among different circuit simulators, while an online tool called JFETlab allows for an easy exploration of device behavior. The new compact model of JFETs addresses a variety of needs, from device design and analysis, to circuit design of low-noise analog/RF and low-power digital applications based on JFETs. The CJM model furthermore is applicable to wide-bandgap semiconductors, such as SiC or GaN, which are particularly suitable for harsh environments.

REFERENCES

[1] M. Manghisoni *et al.*, "JFET front end circuits integrated in a detector grade silicon substrate," *IEEE Trans. Nucl. Sci.*, vol. 50, no. 4, pp. 942–947, Aug. 2003. doi: 10.1109/NSSMIC.2002.1239280.

[2] D. A. Fleischer *et al.*, "CMOS-integrated low-noise junction field-effect transistors for bioelectronic applications," *IEEE Electron Device Lett.*, vol. 39, no. 7, pp. 931–934, Jul. 2018. doi: 10.1109/LED.2018.2844545.

[3] Y. Shi *et al.*, "A cost-competitive high performance junction-FET (JFET) in CMOS process for RF and analog applications," in *Proc. IEEE Radio Freq. Integr. Circuit Symp. (RFIC)*, Anaheim, CA, USA, May 2010, pp. 237–240. doi: 10.1109/RFIC.2010.5477348.

[4] K. Nidhi and M.-D. Ker, "A CMOS-process-compatible low-voltage junction-FET with adjustable pinch-off voltage," *IEEE Trans. Electron Devices*, vol. 64, no. 7, pp. 2812–2819, Jul. 2017. doi: 10.1109/TED.2017.2706423.

[5] A. Qiang, S. Subramaniam, M. Ong, and C. R. Manoj, "A cost-competitive low noise junction-FET (JFET) for high-precision analog application," in *Proc. 25th Int. Conf. Noise Fluctuations (ICNF)*, Lausanne, Switzerland, Jun. 2019, pp. 184–187.

[6] J. B. Jackson, D. Kapoor, and M. S. Miller, "Junction field effect transistors for nanoelectronics," *IEEE Trans. Nanotechnol.*, vol. 8, no. 6, pp. 749–757, Nov. 2009. doi: 10.1109/TNANO.2008.2011383.

[7] A. K. Kapoor *et al.*, "Complementary logic with 60 nm poly gate JFET for 0.5 V operation," *Electron. Lett.*, vol. 46, no. 11, p. 783, May 2010. doi: 10.1049/el.2010.0742.

[8] A. K. Kapoor, "Electrostatics of JFET at 6 nm channel length: A simulation study," *Electron. Lett.*, vol. 47, no. 15, pp. 870–871, Jul. 2011. doi: 10.1049/el.2011.1420.

[9] P. G. Neudeck, D. J. Spry, L. Chen, N. F. Prokop, and M. J. Krasowski, "Demonstration of 4H-SiC digital integrated circuits above 800 °C," *IEEE Electron Device Lett.*, vol. 38, no. 8, pp. 1082–1085, Aug. 2017. doi: 10.1109/LED.2017.2719280.

[10] M. Nakajima, M. Kaneko, and T. Kimoto, "Normally-off 400 °C operation of n- and p-JFETs with a side-gate structure fabricated by ion implantation into a high-purity semi-insulating SiC substrate," *IEEE Electron Device Lett.*, vol. 40, no. 6, pp. 866–869, Jun. 2019. doi: 10.1109/LED.2019.2910598.

[11] B. M. M. Tripathi and S. P. Das, "Performance evaluation of normally ON/OFF junctionless vertical channel GaN FET," *Appl. Phys. A*, vol. 124, pp. 593–600, Sep. 2018. doi: 10.1007/s00339-018-2018-2.

[12] W. M. C. Sansen and C. J. M. Das, "A simple model of ion-implanted JFET's valid in both the quadratic and the subthreshold regions," *IEEE J. Solid-State Circuits*, vol. SSC-17, no. 4, pp. 658–666, Aug. 1982. doi: 10.1109/JSSC.1982.1051794.

[13] H. Ding, J. J. Liou, K. Green, and C. R. Cirba, "A new model for four-terminal junction field-effect transistors," *Solid-State Electron.*, vol. 50, no. 3, pp. 422–428, 2006. doi: 10.1016/j.sse.2006.01.001.

[14] J. Chang, A. K. Kapoor, L. F. Register, and S. K. Banerjee, "Analytical model of short-channel double-gate JFETs," *IEEE Trans. Electron Devices*, vol. 57, no. 8, pp. 1846–1855, Aug. 2010. doi: 10.1109/TED.2010.2051193.

[15] E. Platania *et al.*, "A physics-based model for a SiC JFET accounting for electric-field-dependent mobility," *IEEE Trans. Ind. Appl.*, vol. 47, no. 1, pp. 199–211, Jan./Feb. 2011. doi: 10.1109/TIA.2010.2090843.

[16] K. Xia, C. C. McAndrew, and B. Grote, "Dual-gate JFET modeling II: Source pinchoff voltage and complete I_{DS} modeling formalism," *IEEE Trans. Electron Devices*, vol. 63, no. 4, pp. 1416–1422, Apr. 2016. doi: 10.1109/TED.2016.2521759.

[17] S. Banáš, V. Paňko, J. Dobeš, P. Hanyš, and J. Divín, "Comprehensive behavioral model of dual-gate high-voltage JFET and pinch resistor," *Solid-State Electron.*, vol. 123, pp. 133–142, Sep. 2016. doi: 10.1016/j.sse.2016.05.001.
[18] N. Makris, F. Jazaeri, J.-M. Sallese, R. K. Sharma, and M. Bucher, "Charge-based modeling of long-channel symmetric double-gate junction FETs—Part I: Drain current and transconductances," *IEEE Trans. Electron Devices*, vol. 65, no. 7, pp. 2744–2750, Jul. 2018. doi: 10.1109/TED.2018.2838101.
[19] N. Makris, F. Jazaeri, J.-M. Sallese, and M. Bucher, "Charge-based modeling of long-channel symmetric double-gate junction FETs—Part II: Total charges and transcapacitances," *IEEE Trans. Electron Devices*, vol. 65, no. 7, pp. 2751–2755, Jul. 2018. doi: 10.1109/TED.2018.2838090.
[20] N. Makris, M. Bucher, F. Jazaeri, and J.-M. Sallese, "A compact model for static and dynamic operation of symmetric double-gate junction FETs," in *Proc. Eur. Solid-State Device Res. Conf. (ESSDERC)*, Dresden, Germany, Sep. 2018, pp. 238–241. doi: 10.1109/ESSDERC.2018.8486848.
[21] F. Jazaeri and J.-M. Sallese, *Modeling Nanowire and Double-Gate Junctionless Field-Effect Transistors*. Cambridge, U.K.: Cambridge Univ. Press, 2018. doi: 10.1017/9781316676899.
[22] C. C. McAndrew *et al.*, "Best practices for compact modeling in Verilog-A," *IEEE J. Electron Devices Soc.*, vol. 3, no. 5, pp. 383–396, Sep. 2015. doi: 10.1109/JEDS.2015.2455342.
[23] *ATLAS User's Manual*, SILVACO Inc., Santa Clara, CA, USA, 2018.
[24] J.-M. Sallese, M. Bucher, F. Krummenacher, and P. Fazan, "Inversion charge linearization in MOSFET modeling and rigorous derivation of the EKV compact model," *Solid-State Electron.*, vol. 47, no. 4, pp. 677–683, 2003. doi: 10.1016/S0038-1101(02)00336-2.
[25] F. Jazaeri and J.-M. Sallese, "Charge-based EPFL HEMT model," *IEEE Trans. Electron Devices*, vol. 66, no. 3, pp. 1218–1229, Mar. 2019. doi: 10.1109/TED.2019.2893302.
[26] J.-M. Sallese, N. Chevillon, C. Lallement, B. Iniguez, and F. Pregaldiny, "Charge-based modeling of junctionless double-gate field-effect transistors," *IEEE Trans. Electron Devices*, vol. 58, no. 8, pp. 2628–2637, Aug. 2011. doi: 10.1109/TED.2011.2156413.
[27] R. D. Trevisoli, R. T. Doria, M. de Souza, and M. A. Pavanello, "A physically-based threshold voltage definition, extraction and analytical model for junctionless nanowire transistors," *Solid-State Electron.*, vol. 90, pp. 12–17, Dec. 2013. doi: 10.1016/j.sse.2013.02.059.
[28] T. A. Oproglidis *et al.*, "Analytical drain current compact model in the depletion operation region of short-channel triple-gate junctionless transistor," *IEEE Trans. Electron Devices*, vol. 64, no. 1, pp. 66–72, Jan. 2017. doi: 10.1109/TED.2016.2632753.
[29] *2SK30A TOSHIBA Field Effect Transistor, Silicon N Channel Junction Type*, Datasheet, TOSHIBA Corporat., Japan, 2003.
[30] N. Makris, K. Zekentes, and M. Bucher, "Compact modeling of SiC and GaN junction FETs at high temperature," *Mater. Sci. Forum*, vol. 963, pp. 683–687, Jul. 2019. doi: 10.4028/www.scientific.net/MSF.963.683.
[31] N. Makris, M. Bucher, F. Jazaeri, and J.-M. Sallese. (2018). *JFETLab: An Online Simulation Tool for Double Gate Symmetrical JFETs*. [Online]. Available: https://nanohub.org/resources/jfetlab

NIKOLAOS MAKRIS received the M.Sc. degree in electronic and computer engineering from the Technical University of Crete, Chania, Greece, in 2011, where he is currently pursuing the Ph.D. degree with the School of Electrical and Computer Engineering. He has been cooperating with the Institute of Electronic Structure and Laser, Foundation for Research and Technology Hellas, developing SiC FETs. His research interests include the characterization and compact modeling of advanced FETs. He was a recipient of the Best Paper Award from ESSDERC in 2018.

MATTHIAS BUCHER received the Ph.D. degree from the Ecole Polytechnique Fédérale de Lausanne, Lausanne, Switzerland, in 1999. He is currently an Associate Professor with the School of Electrical and Computer Engineering, Technical University of Crete, Chania, Greece. His current research interests include the design of low-power, low-voltage and high-frequency integrated circuits, and the characterization and compact modeling of advanced solid-state devices including noise, variability, and high-frequency effects. He was a recipient of the Best Paper Award from ESSDERC in 2018.

FARZAN JAZAERI received the Ph.D. degree in microelectronics and microsystems from the Ecole Polytechnique Fédérale de Lausanne, Lausanne, Switzerland, in 2015, where he joined as a Research Scientist and a Project Leader with Integrated Circuits Laboratory. His current research interests include solid state physics and advanced semiconductor devices for operation within extreme harsh environments, i.e., high energy particle background and cryogenic temperatures for space applications and quantum computations. He was a recipient of the Best Paper Award from ESSDERC in 2018.

JEAN-MICHEL SALLESE received the Ph.D. degree in physics from the University of Nice Sophia Antipolis, Nice, France. He joined the Ecole Polytechnique Fédérale de Lausanne, Lausanne, Switzerland, and was appointed as a Maitre d'Enseignement et de Recherche. His group (Electron Device Modeling and Technology Laboratory) has dedicated attention to solid state physics and modeling of field-effect transistors, radiation damage in integrated circuits in collaboration with CERN, and heterostructure HEMT devices. He was a recipient of the Best Paper Award from ESSDERC in 2018.